PROCEEDINGS, 41st Workshop on Geothermal Reservoir Engineering
Stanford University, Stanford, California, February 22-24, 2016
SGP-TR-209

Characterizing Pressure Transients in Shear-Stimulated Fracture Networks

Thein Htaik and Mark W. McClure

Department of Petroleum and Geosystems Engineering, The University of Texas at Austin

Email: mgtheinhtaik@utexas.edu

Keywords: pressure transients, shear-stimulated fracture networks, tendency for shear stimulation test

ABSTRACT

The classical theory of hydraulic fracturing is that injection creates a single, planar fracture that propagates through the formation. However, a variety of observations indicate that injection can create a network of fractures, especially in Enhanced Geothermal Systems (EGS) and in shale. Since 1980s, it has been recognized that an important mechanism of stimulation in EGS is shear stimulation, the stimulation of natural fractures from induced slip on preexisting fractures. The tendency for shear stimulation (TSS) test has been proposed as a way of measuring the ability of a formation to experience shear stimulation. In a TSS test, fluid is injected into a well while maintaining the bottomhole fluid pressure modestly lower than the minimum principal stress. Under these conditions, injection pressure is high enough to cause shear stimulation but low enough to avoid propagating hydraulic fractures through the formation. This test isolates the effect of shear stimulation because it should be the only possible mechanism for increasing permeability (unless thermal fracturing occurs). In this study, a discrete fracture network simulator, CFRAC, is used to study pressure transients in shear-stimulated fracture networks. CFRAC takes into account both fluid flow and the stresses induced by fracture deformation. We investigate pressure transient techniques specifically designed to interrogate properties of shear-stimulated fracture networks in unconventional resources. Analytical techniques developed to characterize pressure transients and properties of shear-stimulated fracture networks are compared against the synthetic data sets generated by CFRAC.

1. INTRODUCTION

A variety of data suggests that hydraulic stimulation in unconventional resources often results in the formation of a complex fracture network (Fisher et al., 2004; Bowker, 2007; Gale et al., 2007; Cipolla et al., 2008; King, 2010). There has been considerable discussion about the processes that cause fracture network complexity.

One process that can create complexity is shear stimulation of natural fractures (Pine and Batchelor, 1984; Murphy and Fehler, 1986). Increase in fluid pressure causes slip on preexisting fractures, which experience increase in transmissivity. Fluid injection does not generally form new shear fractures because of the high compressive strength of intact rock (except in unconsolidated formations) (Olson et al., 2009), and so "shear stimulation" refers to induced slip on preexisting fractures, not formation of new shear fractures. McClure and Horne (2014a) pointed out that shear stimulation can only be effective if several conditions are in place: the natural fracture network must be percolating, experience transmissivity enhancement with slip, and contain fractures well-oriented to slip at elevated fluid pressure.

Another process that can create complexity is termination of propagating hydraulic fractures against natural fractures and other preexisting planes of weakness (Warpinski and Teufel, 1987; Warpinski et al., 1993; Mahrer, 1999; Jeffrey et al., 2009; Chuprakov et al., 2013). Termination occurs due to mechanical interference, as slip on the natural fracture blunts the stress intensity factor at the crack tip (Renshaw and Pollard, 1995). Termination may force branching of the fracture network and cause fluid to flow through both new and preexisting fractures (McClure et al., 2015).

In Enhanced Geothermal Systems (EGS), hydraulic stimulation is used for exploitation of geothermal energy. It is generally assumed that in EGS, stimulation occurs primarily through shear stimulation (Tester, 2006). However, it has recently been proposed that propagation of hydraulic fractures may be important in some cases (McClure and Horne, 2013; 2014b). There is a need for techniques that can diagnose and characterize the fracture networks created by shear stimulation.

McClure and Horne (2014a) proposed a "tendency for shear stimulation" (TSS) test as a way of determining whether shear stimulation can be an effective mechanism of stimulation in a particular formation. In a TSS test, injection is performed at fluid pressure slightly less than the minimum principal stress. At this pressure, slip should be able to occur on fractures in the formation, but large-scale hydraulic fracture propagation will not occur. If the well does not experience significant increase in injectivity during the TSS test, this indicates that the formation does not have ability to host significant shear stimulation. If injection is performed at pressure greater than the minimum principal stress, it will be ambiguous whether stimulation is due to shear stimulation of natural fractures or formation of hydraulic fractures.

At the Desert Peak EGS project, injection was performed at pressure controlled to be slightly less than the minimum principal stress, effectively a TSS test, and stimulation was minimal and not persistent (Benato et al., 2013; McClure and Horne, 2014a). In contrast, during the stimulation of Well GPK2 at the Soultz EGS project, very large increases in transmissivity were observed from injection pressure that never exceeded the minimum principal stress (Valley and Evans, 2007`).

The objective of this paper is to extend the concept of a TSS test to consider a second injection period, performed after the initial TSS test, to characterize the stimulated fracture network formed during the TSS test.

2. METHODOLOGY

2.1 CFRAC

Numerical simulations were performed using CFRAC (Complex Fracturing ReseArch Code), which is a discrete fracture network simulator that fully couples fluid flow with fracture transmissivity evolution and stresses induced by fracture opening and sliding. CFRAC is described in detail by McClure and Horne (2013) and only a brief overview is described in this section.

Fluid flow and deformation are calculated along each individual fracture. CFRAC can model flow in both preexisting and newly propagating fractures. However, the location of potentially forming hydraulic fractures must be specified in advance.

CFRAC couples fluid flow with stresses induced by fracture deformation and assumes single-phase liquid water, isothermal, and Darcy flow in the fractures. Gravity is neglected but it has a minimal effect on the simulations because variations in fluid density are small. A wellbore storage coefficient, C_w, can be specified.

Fractures are permitted to either open or slide in response to injection. Fractures open when their fluid pressure exceeds their normal stress. Fractures slide according to Coulomb's law. Stresses induced by fracture deformation are calculated with the Shou and Crouch (1995) displacement discontinuity (boundary element) method that uses quadratic basis functions assuming homogeneous, isotropic and linear elastic deformation. The code Hmmvp (Bradley, 2014) is used to very accurately and efficiently approximate the matrices of interaction coefficients that arise from the displacement discontinuity method, which increases the efficiency of the code significantly. Stresses induced by normal displacement discontinuities of closed fractures are neglected. For a crack, these displacements are limited by joint stiffness and are quite small.

The simulations are two-dimensional, and should be interpreted as showing normal faults from the side, viewed in the direction of the maximum horizontal stress. The out-of-plane thickness of the formation, h, was assumed to be 100 m. In this paper, the vertical direction is referred to as the y-axis direction, and the horizontal direction is referred to as the x-axis direction.

Implicit timestepping is used. During every timestep, the fluid pressure and (if the element is opening and/or sliding) opening and sliding displacement discontinuities are calculated to satisfy simultaneously the unsteady-state mass-balance equation and appropriate stress conditions at each element.

Elements may be closed (walls in contact) or open (walls out of contact), depending on whether the fluid pressure has reached the normal stress. If the walls are in contact, Coulomb's law with a constant coefficient of friction is used to determine whether the fracture should slide, and if so, displacements are calculated so that Coulomb's law is satisfied. If walls are out of contact, displacements are calculated so that the walls bear zero shear stress. A radiation-damping term (Rice, 1993; Segall, 2010) is included for shear stress to approximate the effect of inertia at a high slipping velocity (though a high slipping velocity is uncommon if a constant coefficient of friction is used) and to prevent sliding from happening instantaneously.

The Coulomb-failure criterion with a radiation-damping term is (Segall, 2010):

$$|\tau - \eta v| = \mu_f \sigma_n' + S_0 \quad \text{..... (1)}$$

where τ is the shear stress, η is the radiation-damping coefficient, v is the sliding velocity of the fracture, μ_f is the coefficient of friction (assumed constant in this study), S_0 is fracture cohesion, and σ_n' is the effective normal stress, defined as (Segall, 2010):

$$\sigma_n' = \sigma_n - P \quad \text{..... (2)}$$

where P is fluid pressure and compressive stresses are taken to be positive. For fractures with shear stress less than the frictional resistance to slip, shear deformation is assumed to be negligible.

Void aperture is defined as the volume of fluid stored per fracture area. Hydraulic aperture is defined in relation to the fracture transmissivity. Hydraulic aperture is equal to void aperture between two smooth plates but is lower than void aperture for rough surfaces such as rock fractures (Liu, 2005). A "fracture" in a DFN model may represent a crack, but it may also represent a more-complex feature such as a fault zone (Section 2.3.3 in McClure and Horne, 2013). In the latter case, the void aperture may be much larger than the hydraulic aperture, which is the reason why the model allows them to be different.

Nonlinear equations are used to relate fracture stress, fluid pressure and sliding displacement to hydraulic aperture and void aperture of closed natural fractures (modified from Willis-Richards et al., 1996 and Barton et al., 1985):

$$E = \frac{E_0}{1+9\,\sigma_n'/\sigma_{n,Eref}} + D_{E,eff}\,tan\frac{\varphi_{Edil}}{1+9\,\sigma_n'/\sigma_{n,Eref}} \quad \text{..... (3)}$$

$$e = \frac{e_0}{1+9\,\sigma_n'/\sigma_{n,eref}} + D_{e,eff}\,tan\frac{\varphi_{edil}}{1+9\,\sigma_n'/\sigma_{n,eref}} \quad \text{..... (4)}$$

where E_0, $\sigma_{n,Eref}$, φ_{Edil}, e_0, $\sigma_{n,eref}$ and φ_{edil} are specified constants. $D_{E,eff}$ is defined as equal to D if $D < D_{E,eff,max}$ and equal to $D_{E,eff,max}$ otherwise. The constants are allowed to be different for hydraulic aperture, e, and void aperture, E. Non-zero φ_{Edil} corresponds to pore volume dilation with slip, and non-zero φ_{edil} corresponds to transmissivity enhancement with slip.

The cubic law for fracture transmissivity (the product of fracture permeability and hydraulic aperture) is (Witherspoon et al., 1980):

$$T = ke = \frac{e^3}{12} \quad \text{..... (5)}$$

where T is transmissivity and k is permeability.

In the simulations in this paper, it was assumed that no new fractures could form. Even though the injection pressure was less than the minimum principal stress, it was a simplification to neglect fracture propagation because concentrations of tensile stress could locally develop from sliding fractures, causing tensile fractures (Mutlu and Pollard, 2008).

2.2 Approach

In this study, synthetic pressure transients were generated using CFRAC simulations. The transients were created with an experimental injection test sequence, described below. Using the synthetic data sets, we experimented with quantitative and qualitative methods of interpretation. The efficacy of these methods was tested by comparing their predictions against the known properties of the formation from the simulations.

The test sequence is started with a tendency for shear stimulation test. Injection is performed at constant pressure slightly less than the minimum principal stress. Next, the well is shut-in for several weeks to allow the pressure perturbation to dissipate. Finally, injection is performed at a constant low rate, chosen to be low enough that pressure will not increase enough to cause further shear stimulation.

The purpose of the first injection period is to create a region of shear stimulation around the wellbore. The purpose of the second injection period is to generate a pressure transient that can be analyzed with the tools of pressure transient analysis.

2.3 Details of the Simulations

Four simulations were performed (A, B, C, and D). In Simulation A, the shear dilation angle was set to zero, and so fracture sliding did not cause increase in transmissivity. Simulations B-D had the conditions needed for shear stimulation: coupling of slip to transmissivity enhancement, adequate initial transmissivity, a percolating natural fracture network, and natural fractures well-oriented to slip in response to increase in fluid pressure. Simulation B had a lower value of shear dilation angle than Simulations C and D, indicating lower increase in transmissivity with slip. Simulation D had a lower value of E_0 than the other simulations, indicating lower fluid storage in the fractures. Simulation settings used in all of the simulations are given in Table 1, and simulation settings specific to each simulation are given in Table 2.

The fracture networks were generated stochastically. The fracture locations were chosen randomly, and the fracture orientations were assigned using specified orientation statistics. The fractures were oriented approximately 30° clockwise or counterclockwise from the direction of maximum principal stress, making them well-oriented to slip. The wellbore was modeled as a 30 m openhole section.

The simulations were initialized with homogeneous fluid pressure and initial stress. The external boundaries of the simulation were set to be constant pressure boundaries at 32 MPa, the same as the initial fluid pressure. Wellbore storage was neglected.

Simulation settings A, B, C and D each used same injection sequence: injection at a constant pressure of 47 MPa for 12 hours, shut-in for 60 days, and then injection of fluid at 0.02 kg/s for 100 days.

Table 1- Simulation settings used in all simulations

Parameter	Value	Parameter	Value
$D_{e,eff,max}$	0.005 m	μ	1 cp
G	15,000 MPa	ν_p	0.25
e_0	0.0001 m	μ_f	0.6
h	100 m	η	3 MPa/(m/s)
P_{init}	32 MPa	K_{Ic}	3 MPa-$m^{1/2}$
S_0	0.5 MPa	B	1
$\sigma_{n,eref}$	25 MPa	σ_{xx}	50 MPa
$\sigma_{n,Eref}$	25 MPa	σ_{yy}	75 MPa
ϕ_{Edil}	0°	σ_{xy}	0 MPa
C_w	0 m^3/MPa	k	1×10^{-19} m^2

Table 2 - Simulation settings specific to A, B, C and D

Parameter	A	B	C	D
ϕ_{edil}	0°	2.5°	6°	6°
E_0	0.005 m	0.005 m	0.005 m	0.0001 m

3. RESULTS AND DISCUSSION

3.1 Simulations A, B, C and D

Figs 1-4 show the distribution of fluid pressure at the end of the simulation (at the end of the second injection period) in Simulation A, B, C, and D. Figs 5-8 show the distribution of fracture sliding at the end of the simulations, and Figs 9-12 show the distribution of fracture transmissivity at the end of the simulations. In all four simulations, fracture sliding occurred only during the constant pressure injection of the first injection period. The shut-in period after the first injection was very long in order to allow the formation to return nearly initial conditions. The injection rate during the second injection period was low enough that sliding did not occur. Therefore, the distribution of sliding at the end of the simulation (shown in Figs 5-8) is the same as the distribution of sliding at the end of the first injection period. Fracture transmissivity increases with fracture sliding and also increases with increased fluid pressure (Equations 4 and 5).

Simulation A included no shear stimulation since ϕ_{edil} was set to zero, which means that there was no coupling between slip and transmissivity. In Simulations B-D, shear stimulation during the first injection period enabled significantly more fluid to be injected and the formation of a much larger region of the formation where fracture sliding had occurred, compared to Simulation A (Figs 5 and 6). Comparing Simulations B and C, the higher value of shear dilation angle in Simulation C resulted in an even larger stimulated region (Figs 6 and 7). In Simulation D, the void aperture of the natural fractures was smaller, meaning a larger surface area of fractures was needed to contain the injected fluid and there was an even larger region of shear stimulation (Figs 7 and 8).

The distribution of fracture transmissivity at the end of the simulation correlated closely with the region where fracture sliding occurred. In Simulation A, which had no shear stimulation, there was a region near the well of modest increase in fracture transmissivity caused by the direct coupling of fluid pressure with hydraulic aperture (Equation 4). In the simulations with nonzero shear dilation angle, higher fracture transmissivities were possible due to shear stimulation.

At the end of the simulations, the region of increased fluid pressure was roughly the same size in all the simulations. The increase in fluid pressure began to approach the boundaries of the problem domain, which were constant pressure boundaries. However, as discussed below, these evidently did not affect the transients because no indication of the constant pressure boundaries was seen, except possibly at very late time. If the constant pressure boundaries had affected the transient, the derivative curve would have plunged to zero. Comparison of Figs 1-4 and 5-8 shows that by the end of the second injection period, the fluid pressure front extended beyond the region where sliding occurred during the initial injection.

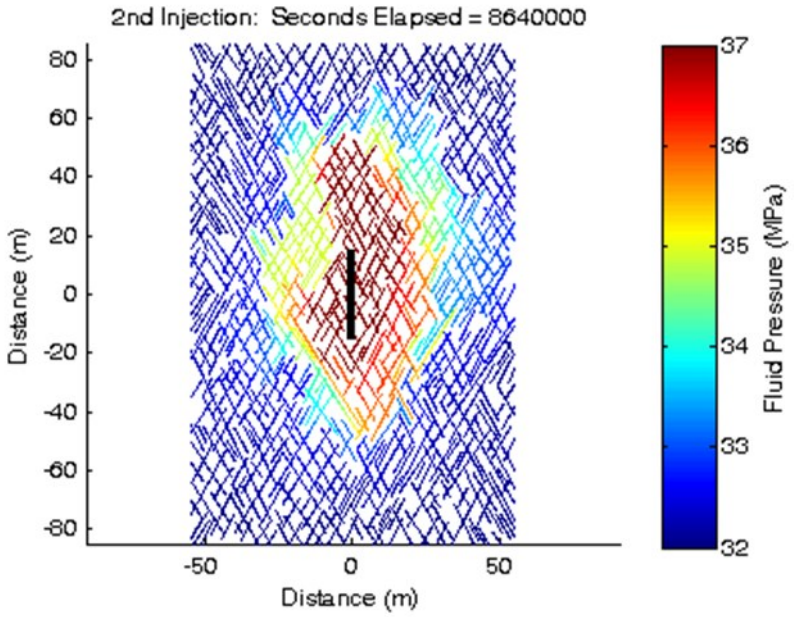

Figure 1: The final pressure distribution for Simulation A. The black line represents the wellbore. The colored lines are natural fractures, with color proportional to fluid pressure.

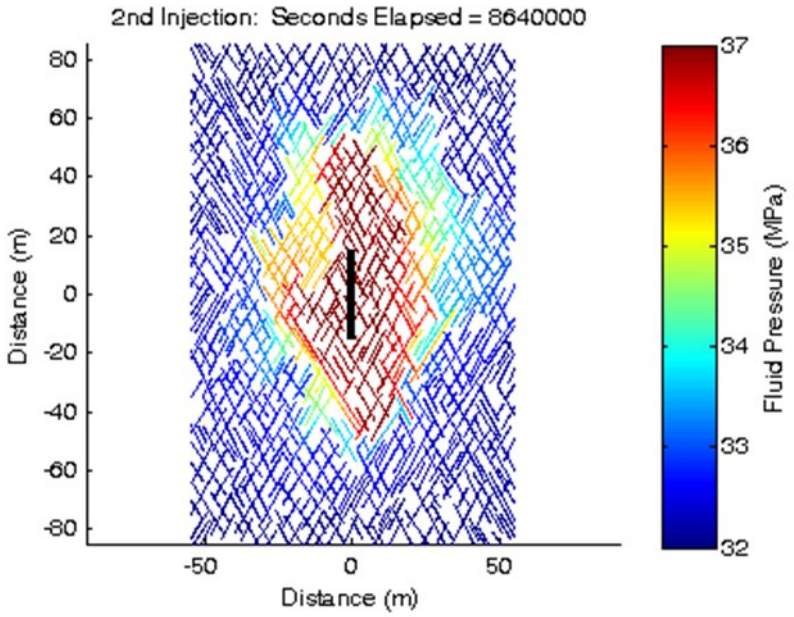

Figure 2: The final pressure distribution for Simulation B. The black line represents the wellbore. The colored lines are natural fractures, with color proportional to fluid pressure.

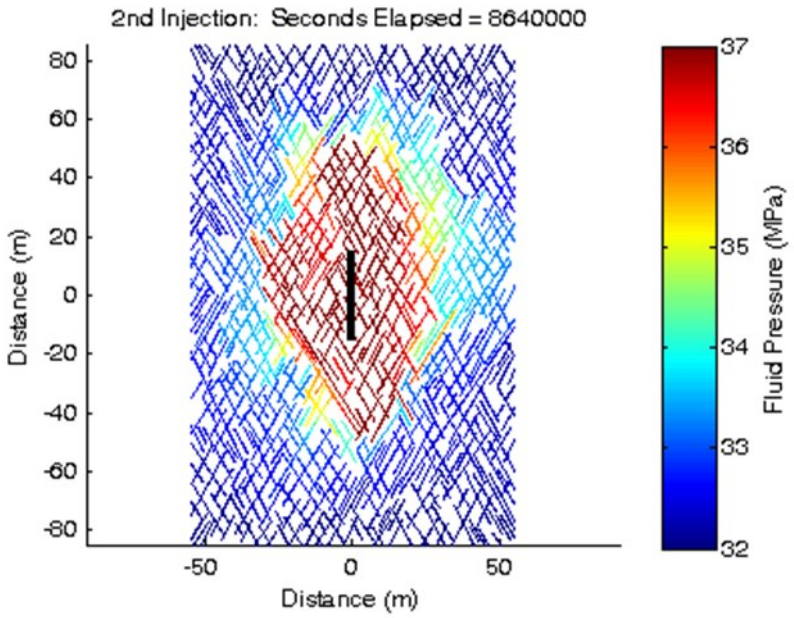

Figure 3: The final pressure distribution for Simulation C. The black line represents the wellbore. The colored lines are natural fractures, with color proportional to fluid pressure.

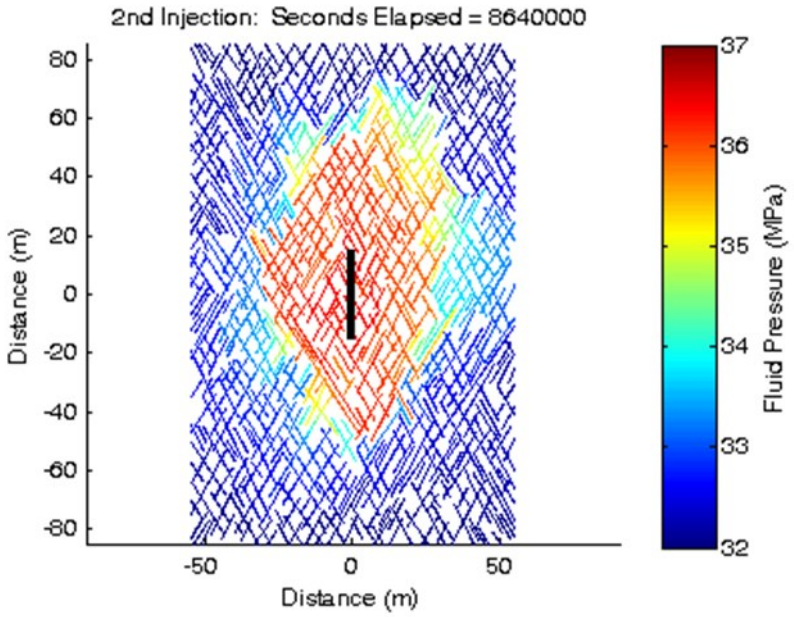

Figure 4: The final pressure distribution for Simulation D. The black line represents the wellbore. The colored lines are natural fractures, with color proportional to fluid pressure.

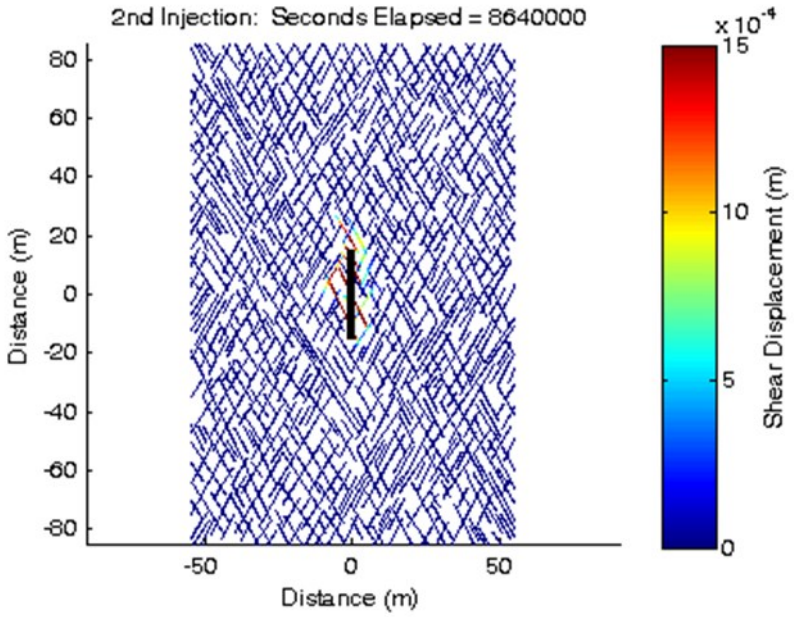

Figure 5: The final shear displacement distribution for Simulation A. The black line represents the wellbore. The colored lines are natural fractures, with color proportional to shear displacement.

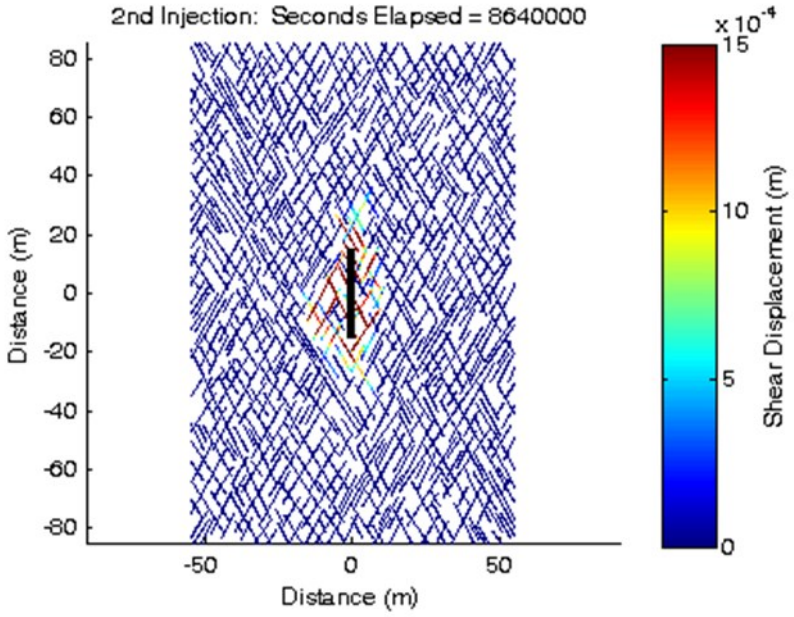

Figure 6: The final shear displacement distribution for Simulation B. The black line represents the wellbore. The colored lines are natural fractures, with color proportional to shear displacement.

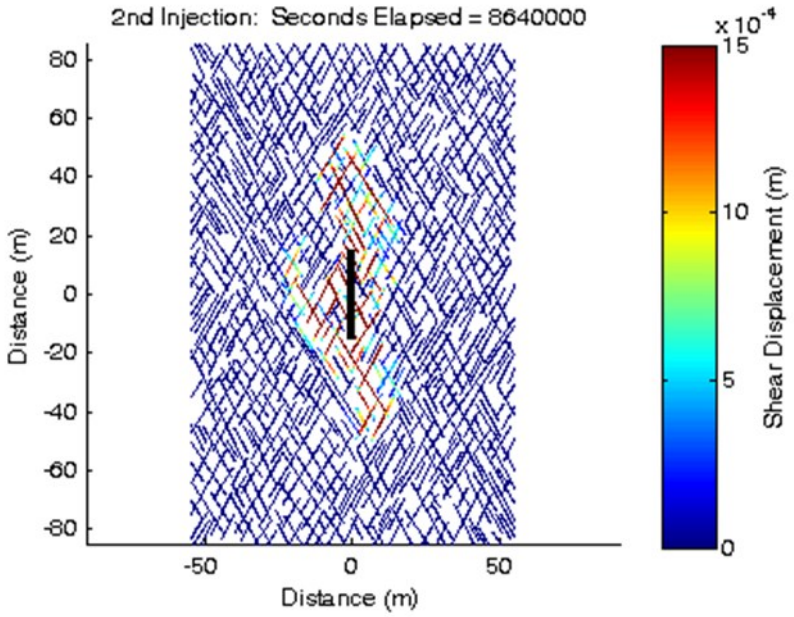

Figure 7: The final shear displacement distribution for Simulation C. The black line represents the wellbore. The colored lines are natural fractures, with color proportional to shear displacement.

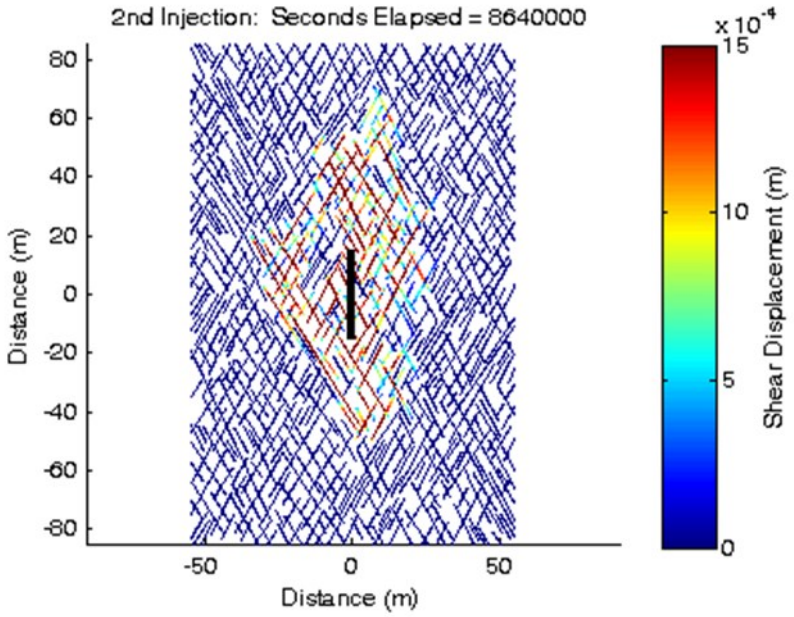

Figure 8: The final shear displacement distribution for Simulation D. The black line represents the wellbore. The colored lines are natural fractures, with color proportional to shear displacement.

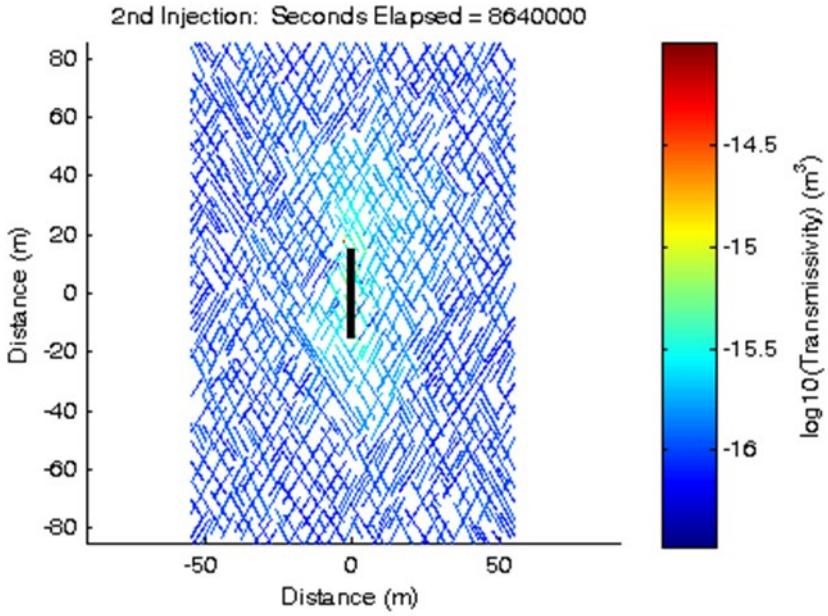

Figure 9: The final transmissivity distribution for Simulation A. The black line represents the wellbore. The colored lines are natural fractures, with color proportional to transmissivity.

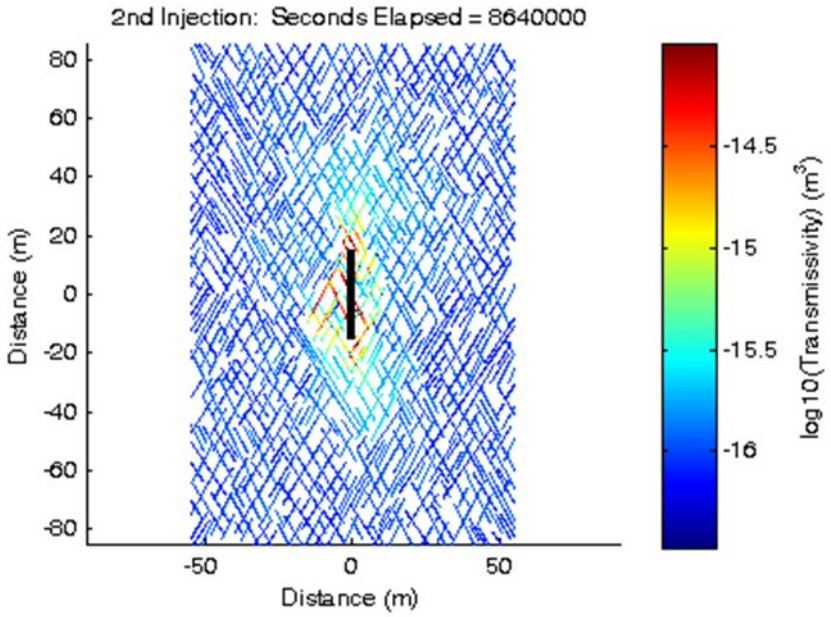

Figure 10: The final transmissivity distribution for Simulation B. The black line represents the wellbore. The colored lines are natural fractures, with color proportional to transmissivity.

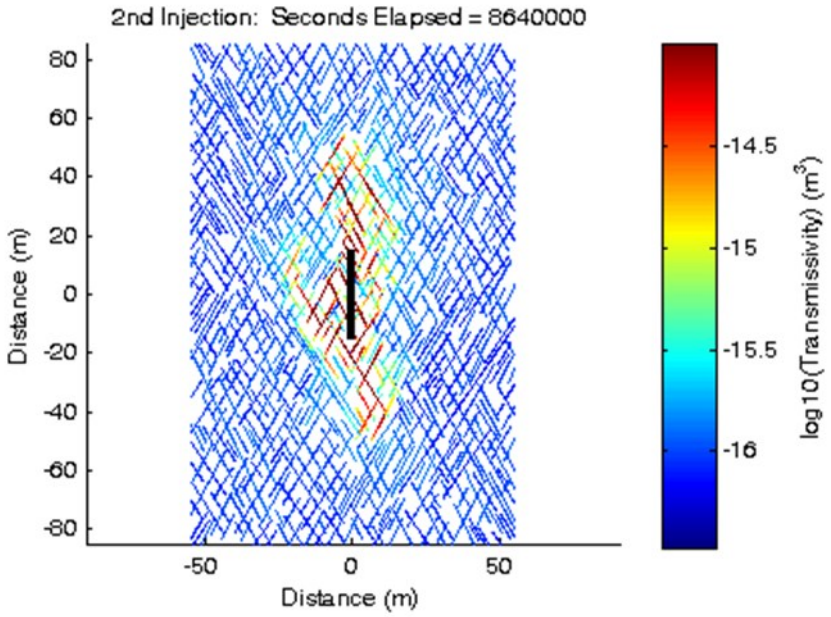

Figure 11: The final transmissivity distribution for Simulation C. The black line represents the wellbore. The colored lines are natural fractures, with color proportional to transmissivity.

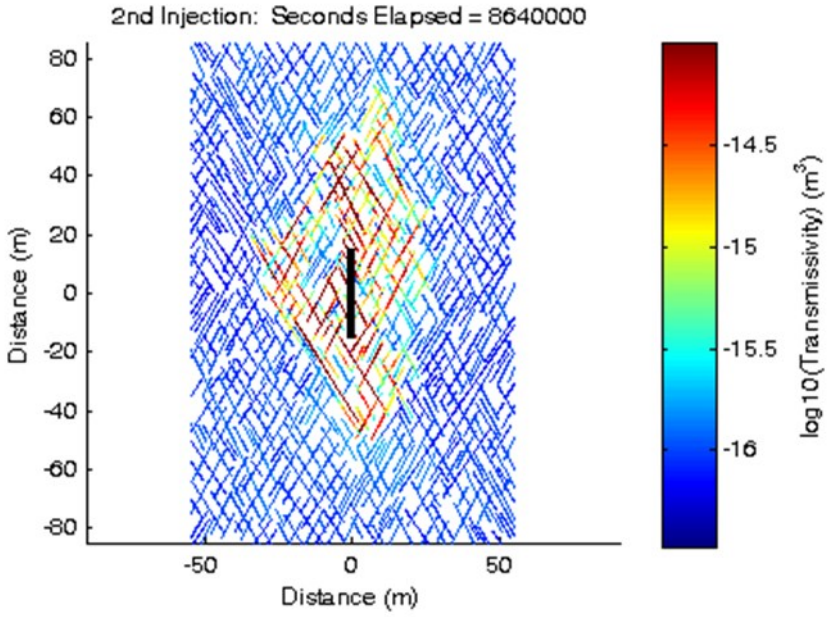

Figure 12: The final transmissivity distribution for Simulation D. The black line represents the wellbore. The colored lines are natural fractures, with color proportional to transmissivity.

Figs 13-16 show the pressure transients from the second injection period (constant rate) in Simulations A-D. All of the simulations began with a period of ½ slope (Fig 13 – 16). At first glance, it is ambiguous whether the ½ slope was caused by fracture linear flow or matrix linear flow. In a fracture linear flow regime, the transient is dominated by flow in the fractures and leakoff is minimal. In a matrix linear flow regime, the pressure gradient in the fractures is minimal and the transient is dominated by flow in the matrix.

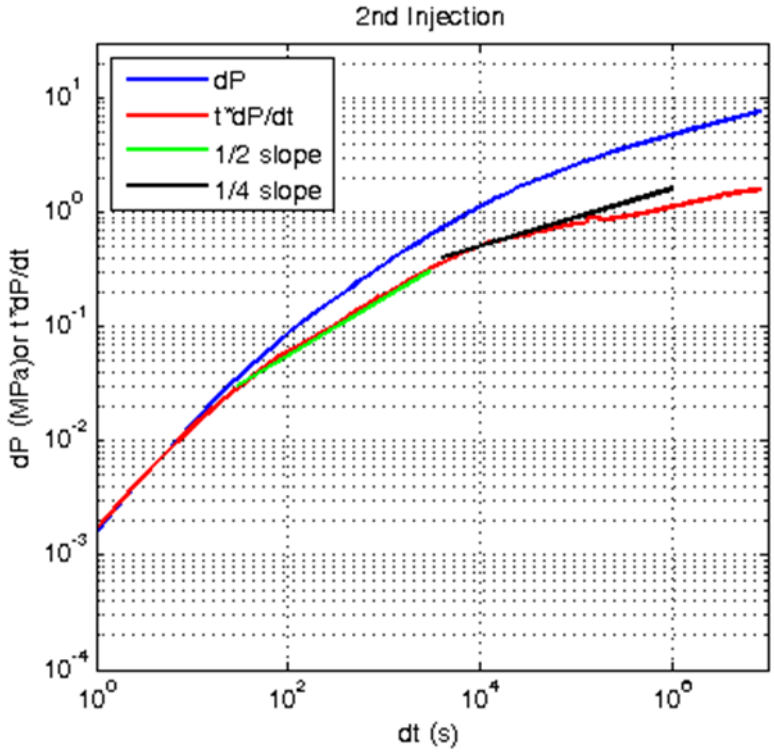

Figure 13: The pressure transient from the 2nd injection in Simulation A

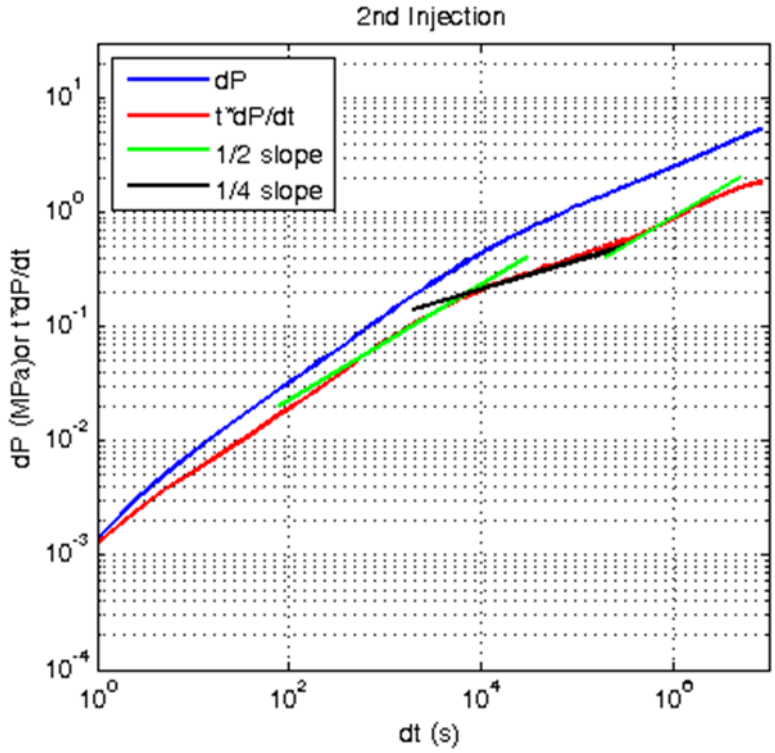

Figure 14: The pressure transient from the 2nd injection in Simulation B

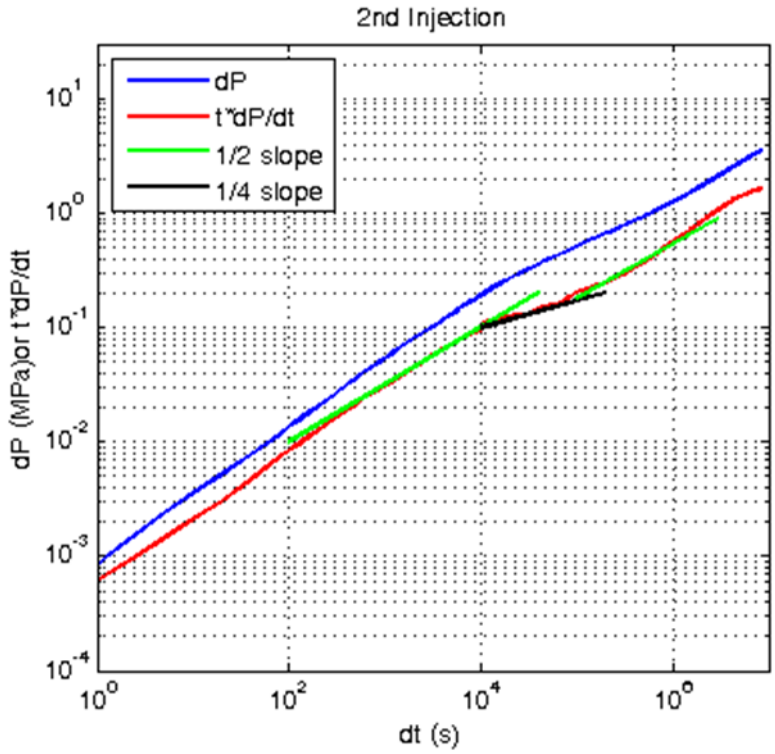

Figure 15: The pressure transient from the 2nd injection in Simulation C

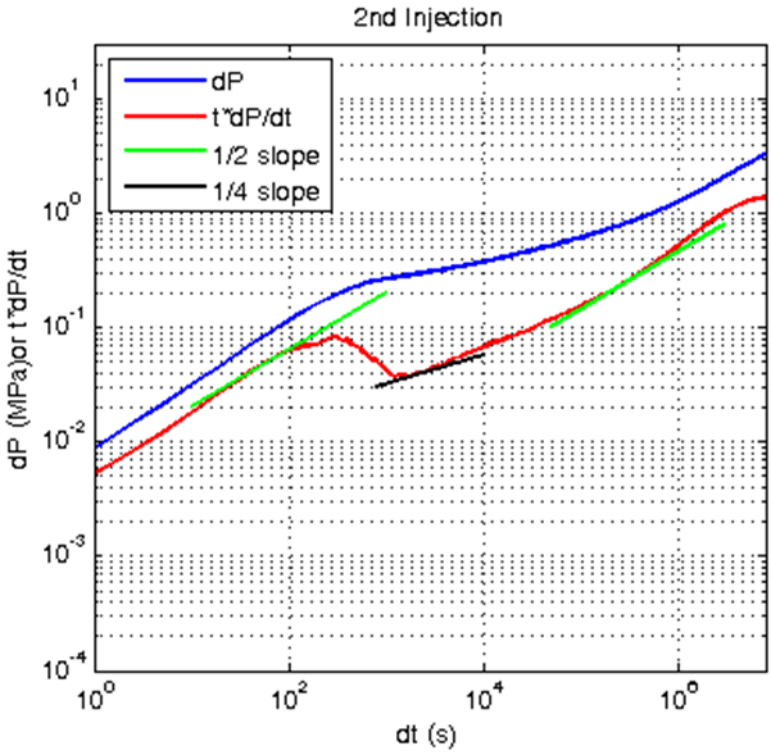

Figure 16: The pressure transient from the 2nd injection in Simulation D

To distinguish between fracture and matrix linear, the change in mass of fluid in the fractures during the second injection was compared with change in mass of fluid in matrix during the second injection. Figure 17 shows this data for Simulation B. The figure shows that at early time, most of the injection fluid is going into the fractures, demonstrating that this early time transient is dominated by fracture linear flow, not matrix linear flow. Similar plots for the other simulations gave the same result- that the early time ½ slope was caused by fracture linear flow. If wellbore storage had been included in the simulations, some or all of the fracture linear period may have been obscured, especially in Simulation D when the fracture linear period was shortest.

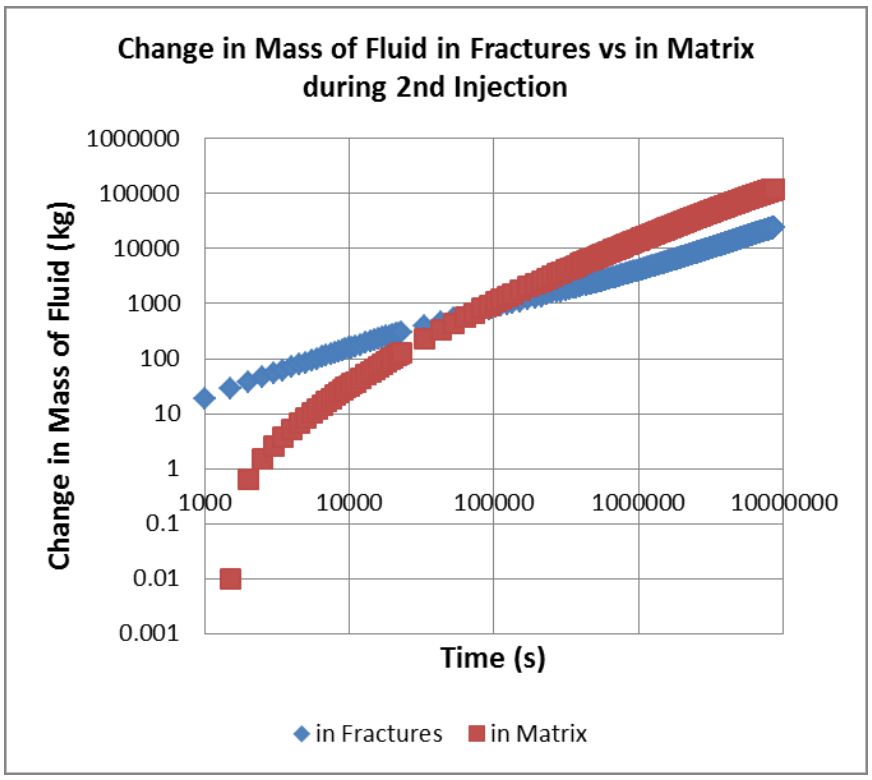

Figure 17: Change in mass of fluid in the fractures and in the matrix during 2nd injection of Simulation B

In Simulations B-D, a second linear flow period occurred at late time. This linear flow period was matrix linear flow. The fracture transmissivity was much higher in the region where fracture sliding had occurred (Fig 9 – 12). In this region, the stimulated natural fractures acted as effectively "infinite conductivity" features at late time, and the transient was dominated by linear leakoff from these fractures into the matrix. A brief bilinear flow period (1/4 slope) may be apparent in the transients between fracture and matrix linear.

In contrast, a second linear flow period is not apparent in the transient for simulation A. At later time, simulation A transitioned to something similar to radial flow. This occurred because there was no shear stimulated region of high fracture transmissivity to act like an infinite conductivity fracture.

The shear dilation angle was larger in Simulation C, compared to Simulation B, which led to a larger shear stimulated region (Fig 10 - 11). The injection pressure was lower in Simulation C, and the stimulated region was larger, but overall the pressure transient was similar. In Simulation D, the fracture void aperture was much smaller. This caused pressure signals to travel much more rapidly through the stimulated fracture network, leading to a much earlier end to the fracture linear period. However, the late-time transient was dominated by leakoff into the matrix, and so the late-time transient in Simulation D appeared similar to Simulation C.

The pressure transients in Simulations B, C and D curved down at very late time as the fluid pressure front extended beyond the stimulated fractures into the surrounding unstimulated fractures (Fig 14 – 16). We confirmed this by watching detailed movies of the simulation result and noting the time when significant fluid pressure perturbation began to travel outside the stimulated region. These times corresponded with the end of the matrix linear flow period in the pressure transients.

3.2 Calculation of stimulated fractured surface area

The pressure transient during the matrix linear flow period can be used to estimate the fracture surface area in the stimulated region. During the matrix linear period, pressure scales with the square root of time. Therefore, a plot of pressure versus the square root of time has a straight line, as shown in Fig 18. The slope of the graph obtained by graphical method can be used to calculate the fracture area.

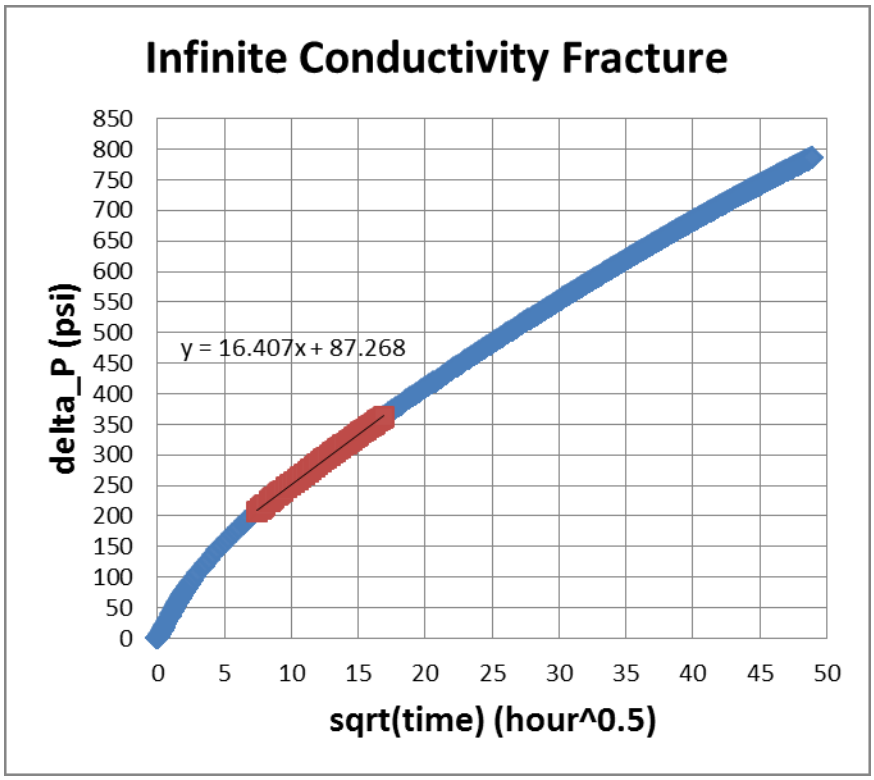

Figure 18: Change in pressure vs. sqrt(time) for 2nd injection of Simulation B

- $\Delta p = \frac{4.06\, q\, B}{L_f\, h}\sqrt{\frac{\mu\, t}{k\, \phi c_t}}$ (Kamal, 2007)
- $L_f = \frac{4.06\, q\, B}{slope\, h}\sqrt{\frac{\mu}{k\, \phi\, c_t}} = \frac{(4.06)(10.87)(1)}{(16.41)(328.084)}\sqrt{\frac{1}{(0.0001)(0.03)(13.1552 \times 10^{-6})}} = 1305\, ft$
- $2L_f = 2 \times 1305\, ft = 2610\, ft = 796\, m$
- $A = 2L_f \times h = 796 \times 100 = 79600\, m^2$
- A = fracture area
- Δp = change in pressure (psi)
- L_f = stimulated half length
- q = flowrate (STB/D)
- B = formation volume factor
- μ = viscosity (cp)
- k = permeability (md)
- ϕ = porosity
- c_t = compressibility (water + porosity) (psi^{-1})
- h = formation thickness (ft)
- t = time (hour)

The calculated value of the stimulated fracture surface area can be compared against the synthetic data sets generated by CFRAC. The stimulated fracture surface area from each simulation can be estimated by calculating the total fracture length where fracture sliding has occurred and multiplying by the out-of-plane thickness. Table 3 provides the results.

Table 3 – Stimulated fracture area of Simulations B, C and D

	Calculated value (m^2)	From simulation data (m^2)
Simulation B	79600	44000
Simulation C	141500	99200
Simulation D	156700	160400

The estimates of the stimulated fracture surface area vary significantly from the calculated values. However, they do provide an order of magnitude estimate. The size of the stimulated fracture surface area could not be estimated from Simulation A because there was no matrix linear flow period (and while fracture slip did occur, there was not a "shear stimulated" region in the simulation).

4. CONCLUSION

The results confirm that a TSS test can be an effective way of determining whether shear stimulation is effective in a particular formation. A subsequent constant pressure injection period can be useful for extracting information about the fracture network created during the TSS test. There should initially be a fracture-dominated transient period. The duration of this fracture-dominated period provides information about the storativity of the fractures in the stimulated region. If the shear stimulation has been effective, there should be a later matrix-linear flow period in the transient. This matrix-linear flow period can be used to provide an order of magnitude assessment of the fracture surface area in the stimulated region (as long as the matrix permeability is known).

The main limitation to this study is that the simulator was two-dimensional. Problem dimensionality can affect pressure transient behavior, and so this study would need to be repeated on a fully 3D DFN simulator before these methods could be applied directly to field data.

ACKNOWLEDGEMENTS

The financial support of the Society of Petroleum Engineers through a New Faculty Research Grant is gratefully acknowledged.

NOMENCLATURE

Parameter	Definition
B	Forchheimer equation constant, unitless
C_w	Wellbore storage, m^3/MPa
D	Cumulative fracture-sliding displacement discontinuity, m
$D_{E,eff}$, $D_{e,eff}$	Effective cumulative fracture-sliding displacement discontinuity, m
$D_{E,eff,max}$, $D_{e,eff,max}$	Maximum effective cumulative fracture-sliding displacement discontinuity, m
e	Hydraulic aperture, m
E	Void aperture, m
e_0	Residual hydraulic aperture, m
E_0	Residual void aperture, m
G	Shear modulus, MPa
h	Out of plane thickness of simulation, m
k	Permeability, m^2
K_{lc}	Fracture toughness, MPa-$m^{1/2}$
P	Fluid pressure, MPa
P_{init}	Initial fluid pressure, MPa
S_0	Fracture cohesion, MPa
T	Transmissivity, m^3
ν_p	Poisson's ratio
η	Radiation damping coefficient, MPa/(m/s)
μ_f	Coefficient of friction, unitless
σ_n	Normal stress, MPa
σ_n'	Effective normal stress, MPa
$\sigma_{n,eref}$	90% fracture closure stress for hydraulic aperture, MPa
$\sigma_{n,Eref}$	90% fracture closure stress for void aperture, MPa
σ_{xx}	Initial principal stress in the x-direction, MPa
σ_{yy}	Initial principal stress in the y-direction, MPa
τ	Shear stress, MPa
ϕ_{edil}	Shear dilation angle for hydraulic aperture, degrees
ϕ_{Edil}	Shear dilation angle for void aperture, degrees

REFERENCES

Barton, N., S. Bandis, K. Bakhtar. 1985. Strength, deformation and conductivity coupling of rock joints. *International Journal of Rock Mechanics and Mining Sciences & Geomechanics Abstracts* 22 (3): 121-140, doi: 10.1016/0148-9062(85)93227-9.

Benato, S., D. M. Reeves, R. Parashar, N. Davatzes, S. Hickman, D. Elsworth, P. Spielman, J. Taron. 2013. Computational investigation of hydro-mechanical effects on transmissivity enhancement during the initial injection phases at the Desert Peak EGS Project, NV. Paper presented at the Thirty-Eighth Workshop on Geothermal Reservoir Engineering, Stanford, CA.

Bowker, Kent A. 2007. Barnett Shale gas production, Fort Worth Basin: issues and discussion. *AAPG Bulletin* 91 (4): 523-533, doi: 10.1306/06190606018.

Bradley, Andrew M. 2014. Software for efficient static dislocation-traction calculations in fault simulators. *Seimological Research Letters* 85 (6), doi: 10.1785/0220140092.

Chuprakov, Dimitry, Olga Melchaeva, Romain Prioul. 2013. Hydraulic fracture propagation across a weak discontinuity controlled by fluid injection. In *Effective and Sustainable Hydraulic Fracturing*, ed. Andrew P. Bunger, John McLennan and Rob Jeffrey, 157-181.

Cipolla, Craig, Norman Warpinski, Michael Mayerhofer, Elyezer Lolon, Michael Vincent. 2008. The relationship between fracture complexity, reservoir properties, and fracture treatment design. Paper SPE 115769 presented at the SPE Annual Technical Conference and Exhibition, Denver, Colorado, USA, doi: 10.2118/115769-MS.

Fisher, M. K., J. R. Heinze, C. D. Harris, Davidson B.M, C. A. Wright, K. P. Dunn. 2004. Optimizing horizontal completion techniques in the Barnett Shale using microseismic fracture mapping. Paper SPE 90051 presented at the SPE Annual Technical Conference and Exhibition, Houston, Texas, doi: 10.2118/90051-MS.

Gale, Julia F. W., Robert M. Reed, Jon Holder. 2007. Natural fractures in the Barnett Shale and their importance for hydraulic fracture treatments. *AAPG Bulletin* 91 (4): 603-622, doi: 10.1306/11010606061.

Jeffrey, Robert, Andrew Bunger, Brice Lecampion, Xi Zhang, Zuorong Chen, Andre van As, David Allison, Willem De Beer, John Dudley, Eduard Siebrits, Marc Thiercelin, Marc Mainguy. 2009. Measuring hydraulic fracture growth in naturally fractured rock. Paper SPE 124919 presented at the SPE Annual Technical Conference and Exhibition, New Orleans, Louisiana, doi: 10.2118/124919-MS.

King, George. 2010. Thirty years of gas shale fracturing: what have we learned? Paper SPE 133456 presented at the SPE Annual Technical Conference and Exhibition, Florence, Italy, doi: 10.2118/133456-MS.

Liu, Enru. 2005. Effects of fracture aperture and roughness on hydraulic and mechanical properties of rocks: implication of seismic characterization of fractured reservoirs. *Journal of Geophysics and Engineering* 2 (1): 38-47, doi: 10.1088/1742-2132/2/1/006.

Mahrer, Kenneth D. 1999. A review and perspective on far-field hydraulic fracture geometry studies. *Journal of Petroleum Science and Engineering* 24 (1): 13-28, doi: 10.1016/S0920-4105(99)00020-0.

McClure, Mark W., Mohsen Babazadeh, Sogo Shiozawa, Jian Huang. 2015. Fully coupled hydromechanical simulation of hydraulic fracturing in three-dimensional discrete fracture networks. Paper SPE 170956 presented at the SPE Hydraulic Fracturing Technology Conference, The Woodlands, TX.

McClure, Mark W., Roland N. Horne. 2013. *Discrete Fracture Network Modeling of Hydraulic Stimulation: Coupling Flow and Geomechanics*: SpringerBriefs in EarthSciences, Springer.

McClure, M. W., R. N. Horne. 2013. Is Pure Shear Stimulation always the mechanism of stimulation in EGS? Paper presented at the Thirty-Eighth Workshop on Geothermal Reservoir Engineering, Stanford, CA.

McClure, Mark W., Roland N. Horne. 2014. Characterizing hydraulic fracturing with a tendency-for-shear-stimulation test. *SPE Reservoir Evaluation & Engineering* 17 (2): 233-243, doi: 10.2118/166332-PA.

McClure, Mark W., Roland N. Horne. 2014. An investigation of stimulation mechanism in Enhanced Geothermal Systems. *International Journal for Rock Mechanics and Mining Sciences* 72: 242-260, doi: 10.1016/j.ijrmms.2014.07.011.

Murphy, H. D., M. C. Fehler. 1986. Hydraulic fracturing of jointed formations. Paper SPE 14088 presented at the International Meeting on Petroleum Engineering, Beijing, China, doi: 10.2118/14088-MS.

Mutlu, O., D. D. Pollard. 2008. On the patterns of wing cracks along an outcrop scale flaw: a numerical modeling approach using complementarity. *Journal of Geophysical Research* 113 (B6), doi: 10.1029/2007JB005284.

Olson, Jon E., Stephen E. Laubach, Robert H. Lander. 2009. Natural fracture characterization in tight gas sandstones: integrating mechanics and diagensis. *Bulletin of the American Association of Petroleum Geologists* 93 (11): 1535-1549, doi: 10.1306/08110909100.

Pine, R. J., A. S. Batchelor. 1984. Downward migration of shearing in jointed rock during hydraulic injections. *International Journal of Rock Mechanics and Mining Sciences & Geomechanics Abstracts* 21 (5): 249-263, doi: 10.1016/0148-9062(84)92681-0.

Renshaw, C. E., D. D. Pollard. 1995. An experimentally verified criterion for propagation across unbounded frictional interfaces in brittle, linear elastic materials. *International Journal of Rock Mechanics and Mining Sciences & Geomechanics Abstracts* 32 (3): 237-249, doi: 10.1016/0148-9062(94)00037-4.

Rice, James R. 1993. Spatio-temporal complexity of slip on a fault. *Journal of Geophysical Research* 98 (B6): 9885-9907, doi: 10.1029/93JB00191.

Segall, Paul. 2010. *Earthquake and Volcano Deformation*. Princeton, N.J., Princeton University Press.

Shou, K. J., S. L. Crouch. 1995. A higher order displacement discontinuity method for analysis of crack problems. *International Journal of Rock Mechanics and Mining Sciences & Geomechanics Abstracts* 32 (1): 49-55, doi: 10.1016/0148-9062(94)00016-V.

Valley, B., K. Evans. 2007. Stress state at Soultz-sous-Forêts to 5 km depth from wellbore failure and hydraulic observations. Paper presented at the Thirty-Second Workshop on Geothermal Reservoir Engineering, Stanford University.

Warpinski, N. R., J. C. Lorenz, P. T. Branagan, F. R. Myal, B. L. Gall. 1993. Examination of a cored hydraulic fracture in a deep gas well, SPE 22876. *SPE Production & Facilities* 8 (3): 150-158, doi: 10.2118/22876-PA.

Warpinski, N. R., L. W. Teufel. 1987. Influence of geologic discontinuities on hydraulic fracture propagation. *Journal of Petroleum Technology* 39 (2): 209-220, doi: 10.2118/13224-PA.

Willis-Richards, J., K. Watanabe, H. Takahashi. 1996. Progress toward a stochastic rock mechanics model of engineered geothermal systems. *Journal of Geophysical Research* 101 (B8): 17481-17496, doi: 10.1029/96JB00882.

Witherspoon, P. A., J. S. Y. Wang, K. Iwai, J. E. Gale. 1980. Validity of cubic law for fluid flow in a deformable rock fracture. *Water Resources Research* 16 (6): 1016-1024, doi: 10.1029/WR016i006p01016.